



Three-dimensional optimization of staggered finned circular and elliptic tubes in forced convection

R.S. Matos^a, T.A. Laursen^b, J.V.C. Vargas^a, A. Bejan^{c,*}

^a Departamento de Engenharia Mecânica, Centro Politécnico, Universidade Federal do Paraná, Caixa Postal 19011, Curitiba, PR 81531-990, Brazil

^b Department of Civil and Environmental Engineering, Duke University, Durham, NC 27708-0287, USA

^c Department of Mechanical Engineering and Materials Science, Duke University, Durham, NC 27708-0300, USA

Received 7 May 2003; accepted 7 October 2003

Abstract

This paper presents a three-dimensional numerical and experimental geometric optimization study to maximize the total heat transfer rate between a bundle of finned tubes in a given volume and external flow, for staggered arrangements of circular and elliptic tubes. Experimental results were obtained for circular and elliptic configurations with twelve tubes, starting with an equilateral triangle configuration, which fitted uniformly into the fixed volume with a resulting optimal dimensionless tube-to-tube spacing of $S/2b = 1.5$, where S is the actual spacing and b is the smaller semi-axis of the ellipse. Several experimental configurations were built by reducing the tube-to-tube spacings, identifying the optimal spacing for maximum heat transfer. Similarly, it was possible to investigate the existence of optima with respect to two other geometric degrees of freedom, such as tube eccentricity and fin-to-fin spacing. The results are reported for air as the external fluid in the laminar regime, for $Re_L = 852$ and 1065 , where L is the swept length of the fixed volume. Circular and elliptic arrangements with the same flow obstruction cross-sectional area were compared on the basis of maximizing the total heat transfer. This criterion allows one to isolate and quantify the heat transfer gain, by studying arrangements with equivalent total pressure drops independently of the tube cross-section shape. This paper continues with three-dimensional numerical optimization results for finned circular and elliptic tubes arrangements, which are validated by direct comparison with experimental measurements. Global optima with respect to tube-to-tube spacing, eccentricity and fin-to-fin spacing ($S/2b \cong 0.5$, $e \cong 0.5$, $\phi_f \cong 0.06$ for $Re_L = 852$ and 1065) were found and reported in dimensionless terms. A relative heat transfer gain of up to 19% is observed in the optimal elliptic arrangement, as compared to the optimal circular one. The heat transfer gain, combined with the relative material mass reduction of up to 32% observed in the optimal elliptic arrangement in comparison to the circular, show that the elliptical tubes arrangement has better overall performance and lower cost than the traditional circular tubes geometry.

© 2003 Elsevier SAS. All rights reserved.

Keywords: Constructal design; Finned tubes; Elliptic tubes; Spacings; Maximal heat transfer density

1. Introduction

The optimization of industrial processes for maximum utilization of the available energy (exergy) has been a very active line of scientific research in recent times. The increase in energy demand in all sectors of the human society requires an increasingly more intelligent use of available energy. Many industrial applications require the use of heat exchangers with tubes arrangements, either finned or non-finned, functioning as heat exchangers in air conditioning systems, refrigeration, heaters, radiators, etc. Such devices have to be designed according to the availability of space

in the device containing them. A measure of the evolution of such equipment, therefore, is the reduction in size, or in occupied volume, accompanied by the maintenance or improvement of its performance. Hence, the problem consists of identifying a configuration that provides maximum heat transfer for a given space, i.e., maximum heat transfer density [1].

Heat exchangers with finned elliptical tubes were studied experimentally by Brauer [2], Bordalo and Saboya [3], Saboya and Saboya [4] and Jang and Yang [5]. These studies showed that elliptical tubes exhibit more heat transfer relative to the circular ones, and, in addition, they exhibit a pressure drop reduction of up to 30%: Rocha et al. [6] developed a hybrid numerical model for finned circular and elliptic tubes arrangements based on energy con-

* Corresponding author.

E-mail address: dalford@duke.edu (A. Bejan).

Nomenclature

a larger ellipse semi-axis..... m
A_c minimum free flow cross-sectional area.... m²
b smaller ellipse semi-axis m
B_a bias limit of quantity *a*
c_p fluid specific heat at constant pressure J·kg⁻¹·K⁻¹
C(\tilde{U}) momentum capacity matrix
D tube diameter m
 \tilde{D} (\tilde{U}) energy capacity matrix
e ellipses eccentricity, *b/a*
F₁, F₂, F₃ momentum force vectors
G energy force vector
H array height m
k fluid thermal conductivity W·m⁻¹·K⁻¹
K_{ij} viscous stiffness matrices (*i, j* = 1, 2, 3)
 \hat{K}_{ij} penalty matrices (*i, j* = 1, 2, 3)
L array length m
 \tilde{L} diffusive matrix
L/2b array length to smaller ellipses axis aspect ratio
m total mass of the arrangement kg
 \tilde{m} dimensionless total mass of the arrangement
 \dot{m}_{ec} fluid mass flow rate entering one elemental channel kg·s⁻¹
n_f number of fins
n_t total number of tubes
N number of tubes in one unit cell
N_{ec} number of elemental channels
p pressure N·m⁻²
P dimensionless pressure
Pe_L Peclet number based on array length
Pr fluid Prandtl number, *v/α*
P_a precision limit of quantity *a*
 \tilde{q} dimensionless overall thermal conductance, Eq. (15)
 \tilde{q}_* dimensionless overall thermal conductance, Eq. (19)
Q overall heat transfer rate W
Q_{ec} heat transfer rate of one elemental channel.. W
Re_D Reynolds number based on tube diameter, *u_∞D/v*
Re_L Reynolds number based on array length, *u_∞L/v*

Re_δ Reynolds number based on fin-to-fin spacing, *u_∞δ/v*
S spacing between rows of tubes, Fig. 1 m
S/D dimensionless spacing between rows of tubes (circular arrangement)
S/2b dimensionless spacing between rows of tubes (elliptic arrangement)
t time s
t_f fin thickness m
t_t tube thickness m
T temperature K
 \bar{T} average fluid temperature K
u₁, u₂, u₃ velocity components m·s⁻¹
U₁, U₂, U₃ dimensionless velocity components
 \tilde{U} dimensionless velocities tripartitioned vector ($\tilde{U}_1, \tilde{U}_2, \tilde{U}_3$) for *X, Y* and *Z* directions, respectively
U_a uncertainty of quantity *a*
W array width m
x, y, z Cartesian coordinates m
X, Y, Z dimensionless Cartesian coordinates

Greek symbols

α thermal diffusivity m²·s⁻¹
γ penalty factor
ε mesh convergence criterion, Eq. (25)
δ fin-to-fin spacing m
θ dimensionless temperature
 $\bar{\theta}$ dimensionless average fluid temperature
ν fluid kinematic viscosity m²·s⁻¹
ρ density kg·m⁻³
φ_f dimensionless fin density in direction *z*

Subscripts

m maximum
opt optimal
out unit cell outlet
s solid tube wall and fin material
w tube surface
1, 2, 3 directions *x, y* and *z*
∞ free stream

servation and on heat transfer coefficients obtained experimentally by a naphthalene sublimation technique through a heat and mass transfer analogy [4,7], and obtained numerically the fin temperature distribution and fin efficiency in one and two row elliptic tube and plate fin heat exchangers. The fin efficiency results were then compared with the results of Rosman et al. [8] for plate fin and circular heat exchangers, and a relative fin efficiency gain of up to 18% was observed with the elliptical arrangement.

Bordalo and Saboya [3] reported pressure drop measurements comparing elliptic and circular tube and plate fin heat exchanger configurations, with one, two and three-row arrangements. Reductions of up to 30% of the loss coefficient (pressure drop coefficient per unit row due only to the presence of the tubes) were observed, in favor of the elliptic configuration. The comparison was performed between circular and elliptic arrangements with the same flow obstruction cross-sectional area, for $200 \leq Re_\delta \leq 2000$ ($1.8 \leq u_\infty \leq 18.2$ m·s⁻¹, with $\delta = 1.65$ mm), which cover the air

velocity range of interest for air conditioning applications. It is further observed that the reduction in pressure drop is higher as Re_δ increases and negligible for $Re_\delta \sim 200$, for the three-row arrangement.

Matos et al. [9], performed a two-dimensional heat transfer analysis of nonfinned circular and elliptic tubes heat exchangers. The finite element method was used to discretize the fluid flow and heat transfer governing equations and a 2-D isoparametric, four-noded, linear element was implemented for the finite element analysis program, FEAP [10]. The numerical results for the equilateral triangle staggering configuration, obtained with the new element were then validated qualitatively by means of direct comparison to previously published experimental results for circular tubes heat exchangers [11]. Numerical geometric optimization results showed a relative heat transfer gain of up to 13% in the optimal elliptical arrangement, as compared to the optimal circular arrangement. This gain, and the heat transfer gains and pressure drop reductions observed in previous studies [2–5] show that the elliptical arrangement has the potential for a considerably better overall performance than the traditional circular one.

The main focus of the present work is on the experimental and numerical geometric optimization of staggered finned circular and elliptic tubes in a fixed volume to obtain global optima with respect to tube-to-tube spacing, eccentricity and fin-to-fin spacing. Unlike Ref. [9], in this paper a three-dimensional numerical optimization procedure for finned circular and elliptic arrangements is used. The numerical results are validated by means of direct comparison to experimental measurements to search the optimal geometric parameters in general staggered finned circular and elliptic configurations for maximum heat transfer. Circular and elliptic arrangements with the same flow obstruction cross-sectional area are then compared on the basis of maximum total heat transfer. Appropriate nondimensional groups are defined and the optimization results are reported in dimensionless charts.

2. Theory

A typical four-row tube and plate fin heat exchanger with a general staggered configuration is shown in Fig. 1. Fowler and Bejan [12] showed that in the laminar regime, the flow through a large bank of cylinders can be simulated accurately by calculating the flow through a single channel, such as that illustrated by the unit cell seen in Fig. 1. Because of the geometric symmetries, there is no fluid exchange or heat transfer between adjacent channels, or at the top and side surfaces. At the bottom of each unit cell, no heat transfer is expected across the plate fin midplane. In Fig. 1, L , H and W are the length, height and width (tube length) of the array, respectively. The fins are identical, where t is the thickness and δ , is the fin-to-fin spacing.

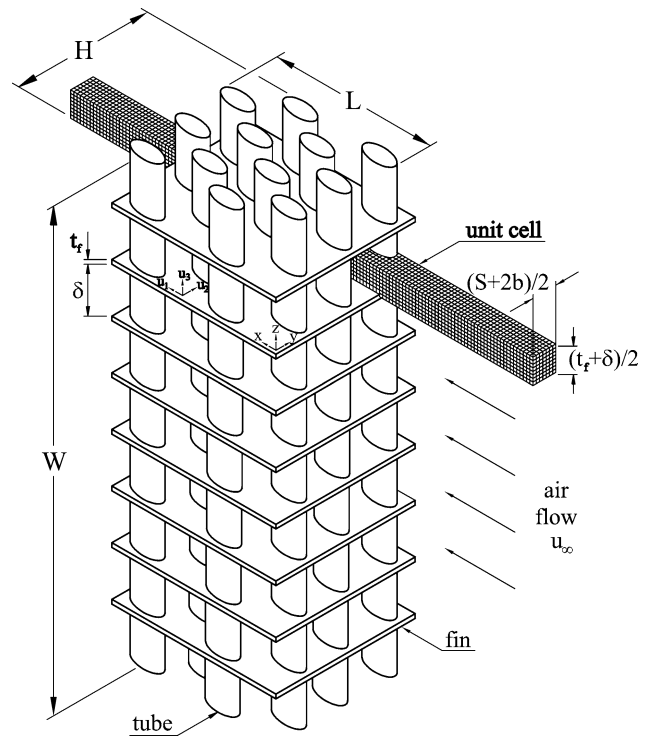


Fig. 1. Arrangement of finned elliptic tubes, and the three-dimensional computational domain.

The governing equations for mass, momentum and energy conservation are simplified in accordance with the assumptions of three-dimensional incompressible steady-state laminar flow with constant properties for a Newtonian fluid, e.g., [13]

$$\frac{\partial U_1}{\partial X} + \frac{\partial U_2}{\partial Y} + \frac{\partial U_3}{\partial Z} = 0 \quad (1)$$

$$U_1 \frac{\partial U_1}{\partial X} + U_2 \frac{\partial U_1}{\partial Y} + U_3 \frac{\partial U_1}{\partial Z} = -\frac{\partial P}{\partial X} + \frac{1}{Re_L} \left[\frac{\partial^2 U_1}{\partial X^2} + \frac{\partial^2 U_1}{\partial Y^2} + \frac{\partial^2 U_1}{\partial Z^2} \right] \quad (2)$$

$$U_1 \frac{\partial U_2}{\partial X} + U_2 \frac{\partial U_2}{\partial Y} + U_3 \frac{\partial U_2}{\partial Z} = -\frac{\partial P}{\partial Y} + \frac{1}{Re_L} \left[\frac{\partial^2 U_2}{\partial X^2} + \frac{\partial^2 U_2}{\partial Y^2} + \frac{\partial^2 U_2}{\partial Z^2} \right] \quad (3)$$

$$U_1 \frac{\partial U_3}{\partial X} + U_2 \frac{\partial U_3}{\partial Y} + U_3 \frac{\partial U_3}{\partial Z} = -\frac{\partial P}{\partial Z} + \frac{1}{Re_L} \left[\frac{\partial^2 U_3}{\partial X^2} + \frac{\partial^2 U_3}{\partial Y^2} + \frac{\partial^2 U_3}{\partial Z^2} \right] \quad (4)$$

$$U_1 \frac{\partial \theta}{\partial X} + U_2 \frac{\partial \theta}{\partial Y} + U_3 \frac{\partial \theta}{\partial Z} = \frac{1}{Pe_L} \left[\frac{\partial^2 \theta}{\partial X^2} + \frac{\partial^2 \theta}{\partial Y^2} + \frac{\partial^2 \theta}{\partial Z^2} \right] \quad (5)$$

The dimensionless variables have been defined based on appropriate physical scales,

$$(X, Y, Z) = \frac{(x, y, z)}{L}, \quad P = \frac{p}{\rho u_\infty^2} \quad (6)$$

$$(U_1, U_2, U_3) = \frac{(u_1, u_2, u_3)}{u_\infty}, \quad \theta = \frac{T - T_\infty}{T_w - T_\infty} \quad (7)$$

$$Re_L = \frac{U_\infty L}{\nu}, \quad Pe_L = \frac{U_\infty L}{\alpha}$$

where (x, y, z) are the Cartesian coordinates, p is the pressure, ρ is the fluid density, u_∞ is the free stream velocity, (u_1, u_2, u_3) are the fluid velocities, T is the temperature, T_∞ is the free stream temperature, T_w is the tube surface temperature, L is the array length in the flow direction, ν is the fluid kinematic viscosity, and α is the fluid thermal diffusivity.

Symmetry allows the computational domain to be reduced to one unit cell, which is represented by the extended domain shown in Fig. 1. The height is $(S/2 + b)$, and the width is $(\delta/2 + t/2)$. The computational domain is composed by the external fluid and half of the solid fin. The solid-fluid interface is included in the solution domain such that mass, momentum and energy are conserved throughout the domain. Eqs. (1)–(5) model the fluid part of the domain. Only the energy equation needs to be solved in the solid part of the domain, by taking into account for the actual properties of the solid material. The dimensionless energy equation for the solid is

$$\frac{\partial \theta}{\partial \tau} = \frac{1}{Re_L} \frac{\alpha_s}{\nu} \left[\frac{\partial^2 \theta}{\partial X^2} + \frac{\partial^2 \theta}{\partial Y^2} + \frac{\partial^2 \theta}{\partial Z^2} \right] \quad (8)$$

where $\tau = t/(L/u_\infty)$ is the dimensionless time, t is the time, and α_s is the solid fin thermal diffusivity. Furthermore, for the steady-state flows considered in this study, $\partial \theta / \partial \tau = 0$.

To complete the problem formulation, the following boundary conditions are then specified for the extended three-dimensional computational domain in agreement with Fig. 2:

$$(A) \quad U_2 = U_3 = 0, \quad U_1 = 1, \quad \theta = 0 \quad (9)$$

$$(B) \text{ and } (C) \quad U_3 = 0, \quad \frac{\partial U_2}{\partial Z} = \frac{\partial U_1}{\partial Z} = \frac{\partial \theta}{\partial Z} = 0 \quad (10)$$

$$(D) \text{ and } (E) \quad U_2 = 0, \quad \frac{\partial U_1}{\partial Y} = \frac{\partial U_3}{\partial Y} = \frac{\partial \theta}{\partial Y} = 0 \quad (11)$$

$$(F) \quad \frac{\partial U_1}{\partial X} = \frac{\partial U_2}{\partial X} = \frac{\partial U_3}{\partial X} = \frac{\partial \theta}{\partial X} = 0 \quad (12)$$

$$(G) \quad U_1 = U_2 = U_3 = 0, \quad \theta = 1 \quad (13)$$

$$(H) \quad U_1 = U_2 = U_3 = 0, \quad \frac{\partial \theta}{\partial Z} = 0 \quad (14)$$

Eq. (13) states that the tube walls are modeled as isothermal, $T_w = \text{constant}$, this in order to account for the presence of a well mixed fluid inside the tubes. In order to represent the actual flow with boundary conditions (A) and (F), two extensions need to be added to the computational domain, upstream and downstream, as shown in Fig. 2. The actual dimensions of these extralengths need to be determined by an iterative numerical procedure, with convergence obtained according to a specified tolerance.

The objective is to find the optimal geometry, such that the volumetric heat transfer *density* is maximized, subject to a volume constraint. The optimization study proceeds

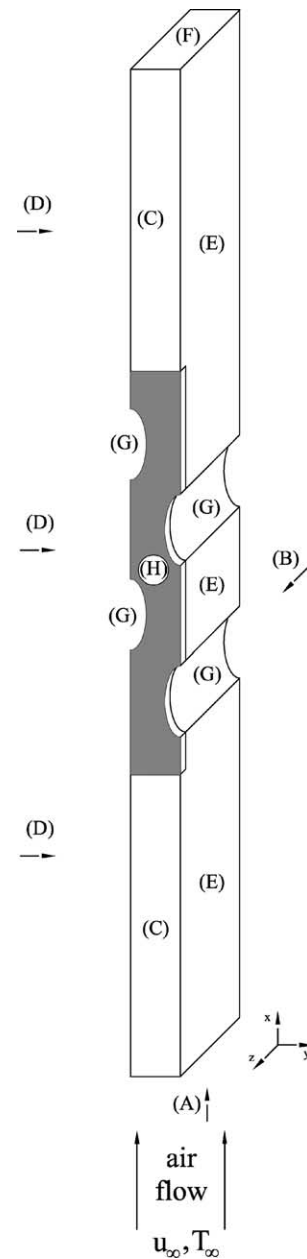


Fig. 2. The boundary conditions of the 3-D computational domain.

with the identification of the degrees of freedom (variables) that allow the maximization of the overall heat transfer rate between the tubes and the free stream, Q . Three geometric degrees of freedom in the arrangement are identified:

- (i) the spacing between rows of tubes, S ;
- (ii) the tubes eccentricity, e , and
- (iii) the fin-to-fin spacing, δ .

These parameters follow from the analysis of the two extremes, small spacings and large spacings. When $S \rightarrow 0$, the mass flow rate in the elemental channel (sum of all unit cells in direction z) decreases and, therefore, $Q \rightarrow 0$. On the other hand, when $S \rightarrow S_{\text{max}}$ (maximum spacing such that the

arrangement with a certain number of elemental channels, N_{ec} , fits in the available space, $L \times H \times W$, the minimum free flow cross sectional area A_c increases, the flow velocity decreases, the heat transfer coefficient decreases, and Q decreases. When $e \rightarrow 0$, the limit of staggered flat plates is represented [14], so $Q \rightarrow Q_{\text{flat plates}}$, and for $e \rightarrow 1$, the limit of circular tubes is reached [9,11], so $Q \rightarrow Q_{\text{circular tubes}}$. This means that the variation of eccentricity allows the heat transfer performance of elliptic tubes to be compared with flat plates and circular tubes, which is one of the objectives of this paper. When $\delta \rightarrow 0$, the mass flow rate in the unit cell decreases, so $Q \rightarrow 0$, and for $\delta \rightarrow \delta_{\text{max}} = W$, the total fin surface area decreases, and Q decreases. The behavior of S , e and δ at the extremes indicate the possibility of maximum Q in the intervals, $0 < S < S_{\text{max}}$, $0 < e < 1$ and $0 < \delta < W$.

A comparison criterion between elliptic and circular arrangements with the same flow obstruction cross-sectional area is adopted, i.e., the circular tube diameter is equal to two times the smaller ellipse semi-axis of the elliptic tube. The reason to adopt this criterion is the possibility to obtain equivalent pressure drops in both arrangements, to be able to quantify the heat transfer gain in the clearest way possible. As pointed out earlier in the text, the difference in pressure drop for elliptic and circular arrangements with identical flow obstruction cross-sectional areas for $Re_\delta < 200$ is negligible [3], which is also verified experimentally in the laboratory for all cases analyzed in this paper.

Once the geometry of the extended computational domain represented by the unit cell of Fig. 2 is specified, Eqs. (1)–(14) deliver the resulting velocities, pressure and temperature fields in the domain. The dimensionless overall thermal conductance \tilde{q} , or volumetric heat transfer density is defined as follows [9,11]:

$$\tilde{q} = \frac{Q/(T_w - T_\infty)}{kLHW/(2b)^2} \tag{15}$$

where the overall heat transfer rate between the finned tubes and the free stream Q is divided by the constrained volume LHW , k is the fluid thermal conductivity, and $2b = D$ is the smaller axis of the ellipse or tube diameter. The first law for one elemental channel requires

$$Q = N_{ec}Q_{ec} = N_{ec}\dot{m}_{ec}c_p(\bar{T}_{\text{out}} - T_\infty) \tag{16}$$

where N_{ec} is the number of elemental channels. The elemental channel is defined as the sum of all unit cells in the direction z . Therefore, $\dot{m}_{ec} = \rho u_\infty[(S + 2b)/2](W - n_f t_f)$ is the mass flow rate entering one elemental channel, c_p is the fluid specific heat at constant pressure, and \bar{T}_{out} is the average fluid temperature at the elemental channel outlet. The number of fins in the arrangement is given by

$$n_f = \frac{W}{t_f + \delta} \tag{17}$$

The dimensionless overall thermal conductance is rewritten using Eqs. (15)–(17),

$$\tilde{q} = \frac{N_{ec}}{2} Pr Re_L \left[\frac{2b}{L} \right]^2 \frac{2b}{H} \left(\frac{S}{2b} + 1 \right) (1 - \phi_f) \bar{\theta}_{\text{out}} \tag{18}$$

where $\phi_f = n_f t_f / W = t_f / (t_f + \delta)$, is the dimensionless fin density in direction z ($0 \leq n_f t_f \leq W$), and Pr the fluid Prandtl number, ν/α . To generalize the results of Eq. (18) for all configurations of the type studied in this work, the dimensionless overall thermal conductance is alternatively defined as follows:

$$\tilde{q}_* = \frac{2}{N_{ec}} \left[\frac{L}{2b} \right]^2 \frac{H}{2b} \tilde{q} = Pr Re_L \left(\frac{S}{2b} + 1 \right) (1 - \phi_f) \bar{\theta}_{\text{out}} \tag{19}$$

The mass fraction occupied by solid material is

$$\tilde{m} = \frac{m}{\rho_s L^3} = \frac{W}{L^3} [n_t \pi (ab(a - t_t)(b - t_t)) + \phi_f(LH - n_t \pi ab)] \tag{20}$$

where t_t is the thickness of the tube wall, and n_t is the total number tubes of the arrangement.

3. Numerical method

The numerical solution to Eqs. (1)–(14) was obtained by using the finite element method [10], giving the velocities and temperature fields in the unit cell of Fig. 2. The first step in the numerical implementation was the elimination of the pressure variable from Eqs. (2)–(4), by using a penalty model, approximating Eq. (1) as [15],

$$\frac{\partial U_1}{\partial X} + \frac{\partial U_2}{\partial Y} + \frac{\partial U_3}{\partial Z} = -\frac{P}{\gamma} \tag{21}$$

where γ is the penalty factor, which must be assumed large enough in order to satisfy mass conservation approximately. The implementation of the finite element method for the solution of Eqs. (1)–(5) and (8) starts from obtaining the variational (weak) form of the problem. The weak form is discretized with an ‘upwind’ scheme proposed by Hughes [16], where it is possible to match the discrete form of the problem to the physical characteristics of the flow. After developing the discrete form of the problem, the resulting algebraic equations are arranged in matrix form for the steady-state three-dimensional problem, as follows:

$$\begin{bmatrix} C(\tilde{U}) & 0 & 0 \\ 0 & C(\tilde{U}) & 0 \\ 0 & 0 & C(\tilde{U}) \end{bmatrix} \begin{Bmatrix} \tilde{U}_1 \\ \tilde{U}_2 \\ \tilde{U}_3 \end{Bmatrix} + \begin{bmatrix} 2K_{11} + K_{22} + K_{33} & K_{12} & K_{13} \\ K_{21} & K_{11} + 2K_{22} + K_{33} & K_{23} \\ K_{31} & K_{32} & K_{11} + K_{22} + 2K_{33} \end{bmatrix} \times \begin{Bmatrix} \tilde{U}_1 \\ \tilde{U}_2 \\ \tilde{U}_3 \end{Bmatrix} + \begin{bmatrix} \hat{K}_{11} & \hat{K}_{12} & \hat{K}_{13} \\ \hat{K}_{21} & \hat{K}_{22} & \hat{K}_{23} \\ \hat{K}_{31} & \hat{K}_{32} & \hat{K}_{33} \end{bmatrix} \begin{Bmatrix} \tilde{U}_1 \\ \tilde{U}_2 \\ \tilde{U}_3 \end{Bmatrix} = \begin{Bmatrix} F_1 \\ F_2 \\ F_3 \end{Bmatrix} \tag{22}$$

$$\tilde{D}(\tilde{U})\tilde{T} + \tilde{L}\tilde{T} = G \tag{23}$$

where $C(\tilde{U})$ is the capacity matrix that contains the advective terms of the momentum equations, which depends nonlinearly on the solution \tilde{U} (tripartitioned vector: \tilde{U}_1 -direction X , \tilde{U}_2 -direction Y and \tilde{U}_3 -direction Z , each one with a number of components equal to the number of unknowns in the mesh); K_{11} , K_{12} , K_{13} , K_{21} , K_{22} , K_{23} , K_{31} , K_{32} and K_{33} are the stiffness matrices with constant coefficients (constant viscosity), that contain the viscous terms of the momentum equations; \hat{K}_{11} , \hat{K}_{12} , \hat{K}_{13} , \hat{K}_{21} , \hat{K}_{22} , \hat{K}_{23} , \hat{K}_{31} , \hat{K}_{32} and \hat{K}_{33} are the penalty matrices, that contain the terms due to the elimination of the pressure variable from the momentum equations by using Eq. (21), which must be computed with reduced integration (one point in each direction with linear shape functions) to avoid locking; $\tilde{D}(\tilde{U})$ is the capacity matrix that contains the advective terms of the energy equation; \tilde{L} is the diffusive matrix with constant coefficients (constant thermal conductivity), which contains the diffusive terms from the energy equation; F_1 , F_2 and F_3 are the force vectors of the momentum equations that contain the field forces and the velocity boundary conditions, and G is the force vector of the energy equation that contains the heat source terms of the energy equation and the temperature boundary conditions.

For the 3-D problem of Fig. 1, the computational domain contains both the external fluid and the solid fin. Thus, the solution of Eq. (8) is also required in order to obtain the complete temperature field. Instead of solving separately for the two entities (fluid and solid) and imposing the same heat flux at the interface solid-fluid, as a boundary condition, the solution is sought for the entire domain, simultaneously, with the same set of conservation equations, imposing zero velocities in the solid fin and the appropriate constant coefficients for the solid fin in the diffusive matrix, \tilde{L} , in Eq. (23), which are obtained from Eq. (8). For the sake of brevity, the mathematical details of the components of the above described matrices are not presented. However, the reader is directed to the work of Reddy and Gartling [15], which was the basis for the formulation implemented computationally in the present study. A Fortran subroutine was written to implement the Navier–Stokes and energy equations in two and three dimensions as isoparametric, four and eight-noded, linear elements, respectively, which were then aggregated to the open code FEAP [10].

4. Experiments

An experimental apparatus was built in the laboratory to produce the necessary experimental data to validate the 3-D numerical optimization of finned arrangements, and to perform the experimental optimization of finned arrangements. Fig. 3 shows the main features of the experimental apparatus utilized in this study. A small scale wind tunnel was built from naval plywood to prevent deformation due to humidity. A test section was designed in modular form as a drawer, to allow the testing many configurations just by changing

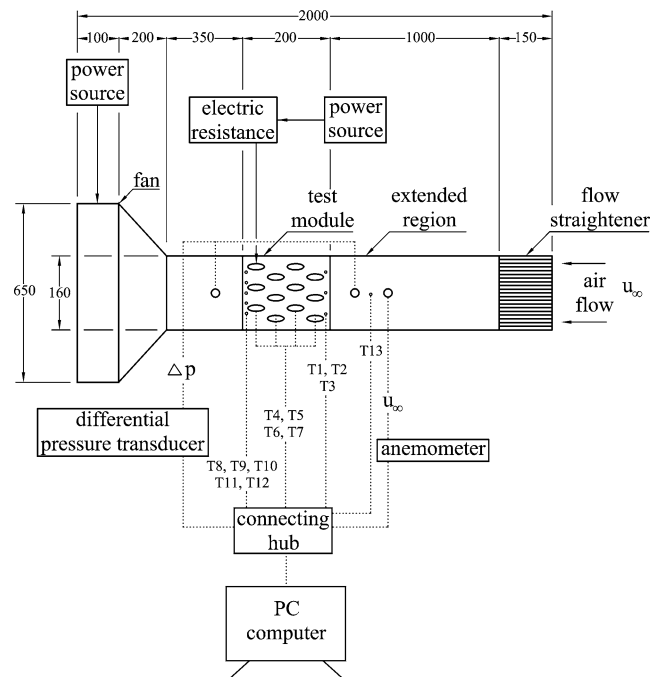


Fig. 3. Experimental apparatus.

the test module, Fig. 3. The internal dimensions of the test section are $175 \times 161 \times 152$ mm. An extended region of 1000 mm was placed before the test section to allow the flow to develop fully before reaching the arrangement. A flow straightener consisting of plastic straws was installed at the entrance of the extended region with the purpose of laminarizing the flow, Fig. 3.

The circular and elliptic tube arrangements were made from copper circular tubes with diameters of 15.875 (5/8"), 22.23 (7/8"), 25.4 (1") and 28.58 mm (11/8") which resulted in tubes with eccentricities $e = 1.0, 0.6, 0.5$ and 0.4 , respectively. The wall thickness was 0.794 mm (1/32") for all eccentricities. To construct the elliptic arrangements, the circular tubes were shaped in the machine shop by using an appropriately designed tool. All the tubes had a length of 172 mm. Electric heaters were placed inside the tubes to simulate the heat flux originated from a hot fluid. All the arrangements had 4 rows of tubes counted in the direction of the external flow, in Fig. 1. Twelve tubes were then assembled, in a wooden drawer, which is the test module shown in Fig. 3. All the fins were made from aluminum plates with dimensions of $150 \times 130 \times 0.3$ mm.

The electric heaters consisted of double step tubular electric resistances with 968Ω , therefore, with a maximum power dissipation of 50 W with 220 V. The electric heaters had a small enough diameter to be fitted into the copper tubes, and were fed with a variable voltage source (30 V, 1.4 A), so that all the arrangements have the same power input.

Twelve high precision thermistors of type YSI 44004 (resistance 2250Ω at 25°C) were placed inside each test module. All the thermistors were placed in the midplane

between the side walls of the wind tunnel and at the midline of the elemental channels. Three thermistors were placed at the inlet (T1–T3), five at the outlet (T8–T12), and four at the tube surfaces in one elemental channel (T4–T7). An additional thermistor (T13) was placed at the midpoint of the extended region to measure the free stream temperature. The thermistors at the inlet and outlet of the arrangement permitted the determination of the vertical variation of temperature in the arrangement. In all the tests performed, the vertical temperatures remained within a $\pm 0.5^\circ\text{C}$ margin with respect to the average (vertical) temperatures calculated at the inlet and outlet. The thermistors on the tube surfaces showed that the temperature difference between tubes in one elemental channel is negligible, namely, within $\pm 0.3^\circ\text{C}$ of the measured average of the four thermistors. Finally, the additional thermistor placed at the extended region measured free stream temperatures within $\pm 0.5^\circ\text{C}$ of the measured average arrangement inlet temperature.

Velocity measurements were made with a vane-type digital anemometer, model HHF 300A (OMEGA Engineering Inc.), which was placed at the extended flow region, as shown in Fig. 3. For the range of 0.1 to $35\text{ m}\cdot\text{s}^{-1}$, the velocity bias limit is $\pm 2.5\%$ of the reading. The free stream velocity was 0.1 and $0.13\text{ m}\cdot\text{s}^{-1}$ in this study. To allow for the continuous variation of the fan velocity, a variable power source with 30 V and maximum current 2 A was used.

The pressure drop measurements were taken with a pressure transducer, model PX137-0.3DV (OMEGA Engineering Inc.), with a nominal range of (0–2068.5 Pa), which was connected to a digital pressure meter, model DP25B-S (OMEGA Engineering Inc.). The differential pressure maximum bias limit is $\pm 1\%$ of the reading. The differential pressure measurements had the purpose of determining the pressure drop across each arrangement in all experiments, Fig. 3.

The experimental work involved the acquisition of temperature data in real time. This task was performed through the utilization of a computational data acquisition system which consisted of a virtual data logger AX 5810 [17] and four multiplexers AX758 [18] which allowed for the sequential data acquisition from 64 channels at time intervals of $1/256\text{ s}$. All the data were processed by a suitable software application to convert the sensors signals in readable temperatures.

The thermistors were calibrated in the laboratory to determine the bias limits. The thermistors were immersed in a constant temperature bath maintained by a bath circulator, and a total of 64 temperature measurements were made between 20 and 80°C , at 10°C increments. The largest standard deviation of these measurements was 0.0005°C , and, therefore, the bias limit was set at $\pm 0.001^\circ\text{C}$ for all thermistors. This bias limit is in agreement with the $\pm 0.0003^\circ\text{C}$ of the same thermistors in a natural convection experiment [19] and with the $\pm 0.0005^\circ\text{C}$ bias limit listed in an instrumentation handbook [20].

The objective of the experimental work was to evaluate the volumetric heat transfer density (or overall thermal conductance) of each tested arrangement by computing \tilde{q}_* with Eq. (19) through direct measurements of $u_\infty(Re_L)$, and \bar{T}_{out} , \bar{T}_w and $T_\infty(\bar{\theta}_{out})$. Five runs were conducted for each experiment. Steady-state conditions were reached after 3 h in all the experiments. The precision limit for each temperature point was computed as two times the standard deviation of the 5 runs [21]. It was verified that the precision limits of all variables involved in the calculation of \tilde{q}_* were negligible in presence of the precision limit of $\bar{\theta}_{out}$. The thermistors, anemometer, properties and lengths bias limits were found negligible in comparison with the precision limit of \tilde{q}_* . As a result the uncertainty of \tilde{q}_* was calculated from

$$\frac{U\tilde{q}_*}{\tilde{q}_*} = \frac{P_{\bar{\theta}_{out}}}{\bar{\theta}_{out}} \quad (24)$$

where $P_{\bar{\theta}_{out}}$ is the precision limit of $\bar{\theta}_{out}$.

For a particular tube and plate fin geometry, the tests started with an equilateral triangle configuration, which filled regularly the fixed volume, with a resulting maximum dimensionless tube-to-tube spacing $S/2b = 1.5$. The spacing between tubes was then reduced stepwise: $S/2b = 1.5, 0.5, 0.25$ and 0.1 . In this interval an optimal spacing was found such that \tilde{q}_* was maximum. All the tested arrangements had the aspect ratio $L/2b = 8.52$.

Two free stream velocities were tested, $u_\infty = 0.1$ and $0.13\text{ m}\cdot\text{s}^{-1}$, corresponding to $Re_L = 852$ and 1065 , respectively. The largest uncertainty calculated according to Eq. (24) in all tests was $U\tilde{q}_*/\tilde{q}_* = 0.048$.

5. Results and discussion

The results obtained in this study are divided in two parts: (i) experimental validation of 3-D numerical results for finned arrangements, and (ii) global optimization results with respect to tube-to-tube spacing, eccentricity and fin density.

The nonlinear system of Eqs. (22) and (23) was solved by the Newton–Raphson method [15], to obtain the velocities and temperatures in the computational domain of Fig. 2. The dimensionless temperatures at the elemental channel outlet were used to compute the dimensionless volumetric heat transfer density \tilde{q}_* defined by Eq. (19).

The numerical results obtained with Eq. (19) are expected to be more accurate than the results that would be obtained by computing the sum of heat fluxes at the tubes surfaces in the elemental channel. The reason is that the former are obtained from the finite element temperature solution, whereas the latter are obtained from temperature spatial derivatives, which are computed from postprocessing the finite element solution. It is well known that the numerical error in the derivative of the solution is larger than the numerical error in the solution itself. To obtain accurate numerical results, several mesh-refinement tests were conducted. The monitored

quantity was the dimensionless overall thermal conductance, computed with Eq. (19), according to the following criterion:

$$\varepsilon = |\tilde{q}_{*,j} - \tilde{q}_{*,j-1}|/|\tilde{q}_{*,j}| \leq 0.02 \quad (25)$$

where j is the mesh iteration index, such that j increases when the mesh is more refined. When the criterion is satisfied, the $j - 1$ mesh is selected as the converged mesh.

Criterion (25) was used to find the appropriate length to the extension domain defined in the unit cell of Fig. 2. The numerical results obtained with an extension L were compared with the numerical results obtained with an extension of $3L/2$, and satisfied the criterion of Eq. (25), by replacing the subscript j with $3L/2$ and the subscript $j - 1$ with L . Therefore, the use of an extension L upstream and downstream of the unit cell was found to be the appropriate to represent the actual flow. Nonregular meshes were used, such that mesh-regions close to the tubes were more refined, to account for the highest gradients in the solution. The last three mesh iterations had (a) 12780 nodes and 9600 elements; (b) 17160 nodes and 13200 elements, and (c) 23166 nodes and 18480 elements, with a relative error below 4% when (a) and (b) are compared, and below 2% when (b) and (c) are compared, according to Eq. (25). Therefore, in all the cases the selected mesh consisted of 17160 nodes and 13200 elements. A sample of converged mesh used in this work is shown in Fig. 4.

The numerical results obtained with the finite element code were validated by direct comparison to experimental results obtained in the laboratory for circular and elliptic arrangements. According to Fig. 1, the dimensions of the fixed volume during experimental optimization were $L = 135.33$ mm, $H = 115.09$ mm, $W = 152$ mm and $D = 2b = 15.875$ mm. All the arrangements had $N_{ec} = 6$ and $N = 4$, where N is the number of tubes in one unit cell.

The numerical and experimental optimization procedures followed the same steps. First, for a given eccentricity, the dimensionless overall thermal conductance, \tilde{q}_* , was computed with Eq. (19), for the range $0.1 \leq S/2b \leq 1.5$. The same procedure was repeated for $e = 0.45, 0.5, 0.6$ and 1 .

Results were obtained for the laminar regime ($Re_L = 852$ and 1065). Figs. 5–8 show the optimization results for finned arrangements ($\phi_f = 0.006$) with respect to tube-to-tube spacing, $S/2b$, for eccentricities $e = 1, 0.6, 0.5$ and 0.45 , respectively. Experimental measurements were not conducted for $e = 0.45$, therefore, only numerical results are shown in Fig. 8. There is good agreement between experimental and numerical results, mainly with respect to the location of the optimal spacing, $S/2b \cong 0.5$, for all eccentricities therefore validating the numerical results. The influence of the variation of Re_L is also investigated. As Re_L increases, \tilde{q}_* increases.

The numerical and experimental double optimization results for finned tubes ($\phi_f = 0.006$) with respect to tube-to-tube spacings and eccentricities are shown in Fig. 9, together with the corresponding experimental results, for

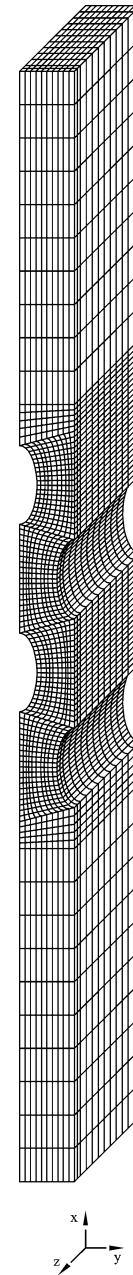


Fig. 4. Sample of converged mesh ($e = 0.5$).

$Re_L = 852$ and 1065 . The $\tilde{q}_{*,m}$ values obtained numerically and experimentally are in good agreement. The agreement is remarkable if we consider that in the experiments the tested arrays had uniform heat flux, and did not contain many cylinders. In the numerical simulations the domain was infinitely wider (i.e., no influence from the wind tunnel walls) and with isothermal tubes. An optimal eccentricity was not obtained experimentally, since an arrangement with $e < 0.5$ was not built. However, the numerical results were validated by the good agreement with the experimental results for $e = 0.5, 0.6$ and 1 . Hence, the numerical results obtained for $e = 0.45$ are also expected to be accurate. At $e = 0.45$, $\tilde{q}_{*,m}$ drops considerably with respect to $e = 0.5$,

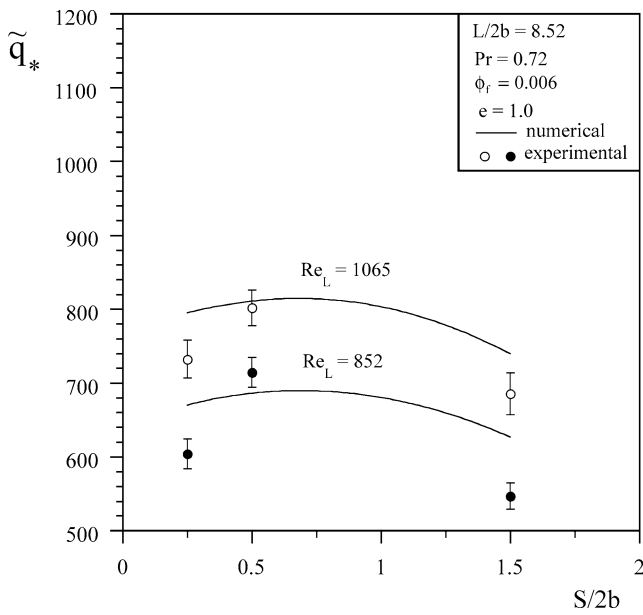


Fig. 5. Numerical and experimental optimization results for finned circular arrangements ($e = 1$).

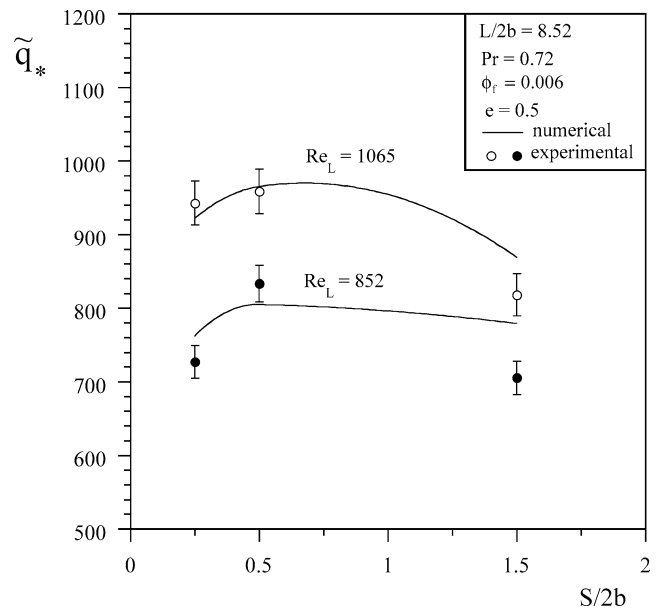


Fig. 7. Numerical and experimental optimization results for finned elliptic arrangements ($e = 0.5$).

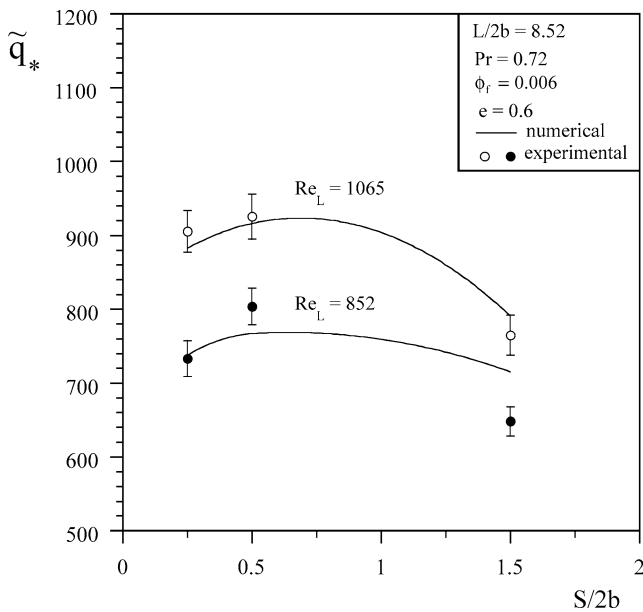


Fig. 6. Numerical and experimental optimization results for finned elliptic arrangements ($e = 0.6$).

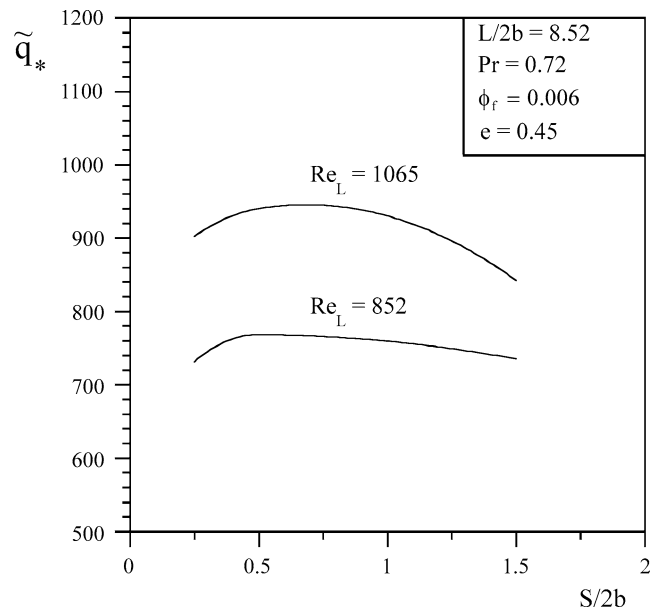


Fig. 8. Numerical optimization results for finned elliptic arrangements ($e = 0.45$).

determining an optimal pair $(S/2b, e)_{opt} = (0.5, 0.5)$ for the twice maximized overall heat transfer $\tilde{q}_{*,mm}$.

Fig. 10 shows an intermediate step in the optimization procedure, to facilitate the comparison between the optimal elliptic configuration with the optimal circular one. Note that $\tilde{q}_{*,m}$ for the elliptic arrangement ($e = 0.5$) optimized with respect to tube-to-tube spacing is higher than $\tilde{q}_{*,m}$ for the circular arrangement ($e = 1$) for all fin densities, ϕ_f . Furthermore, the elliptic configuration requires less fins than the circular one at optimal conditions, i.e., at the optimal pair $(S/2b, \phi_f)_{opt}$. It is possible to determine the

total mass of material in dimensionless terms [via Eq. (20) at $(S/2b, \phi_f)_{opt}$] for both arrangements. The result is that the total dimensionless mass of the optimal elliptic arrangement is 32% smaller than the optimal circular arrangement.

Fig. 11 reports the results of global optimization with respect to the three degrees of freedom, $S/2b$, e and ϕ_f . An optimal set of geometric parameters was determined numerically such that \tilde{q}_* was maximized three times: $(S/2b, e, \phi_f)_{opt} \cong (0.5, 0.5, 0.06)$.

Fig. 12 shows the temperature distribution of plate fins for four-row heat exchangers for circular and elliptic ($e =$

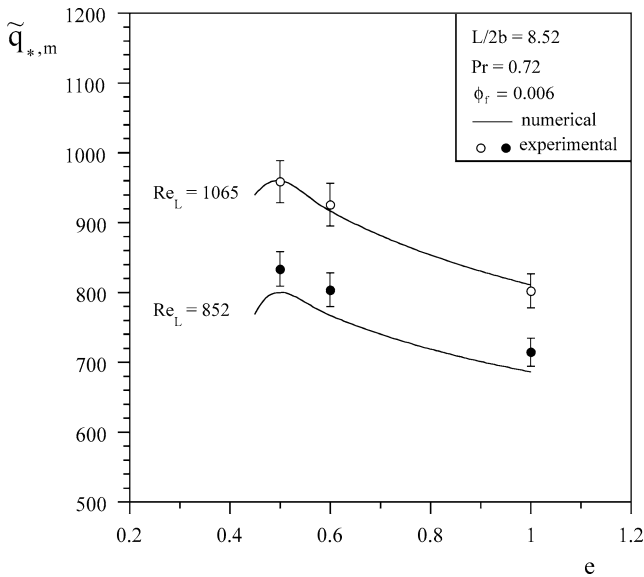


Fig. 9. Numerical and experimental optimization results for finned arrangements.

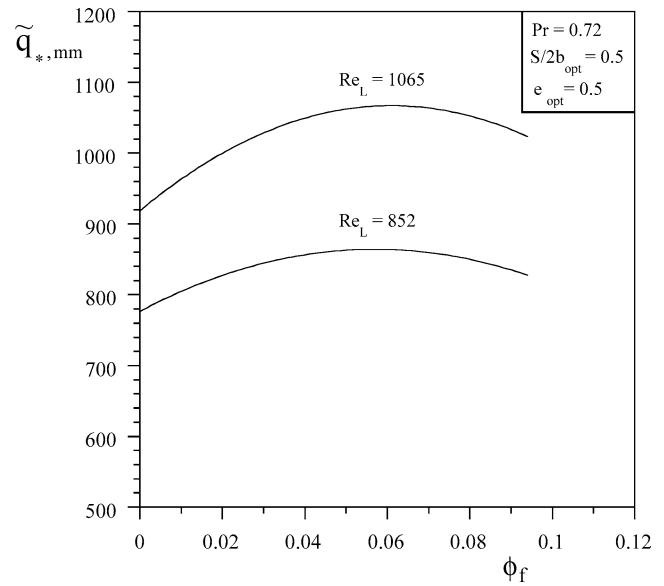


Fig. 11. Numerical global optimization results for finned arrangements.

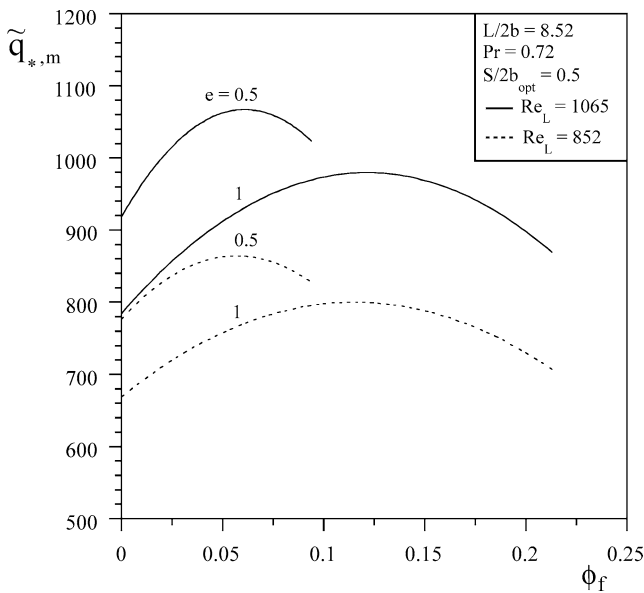


Fig. 10. Comparison of the numerical optimization results for finned circular and elliptic arrangements.

0.5) tubes, $S/2b = 0.5$, $\phi_f = 0.006$, and with $Re_L = 852$. The effect of the variation of eccentricity is observed by comparing cases (a) and (b) in Fig. 12. It is also shown that the elliptical arrangement is more efficient than circular one. This is due to the fact that the fin temperature distribution is more uniform in the elliptic configuration than in the circular one, and closer to tube wall temperature, characterizing a better thermal contact between the tubes and the fluid in the elliptic arrangement.

Because the governing equations are for the laminar regime, the results of Figs. 5–12 were obtained for low Reynolds numbers, or small dimensions, $Re_L = 852$ and 1065 . For higher Reynolds numbers, convergence to numeri-

cal solutions becomes increasingly more difficult, indicating the flow is reaching a regime of transition to turbulence.

6. Conclusions

In this paper, a combined numerical and experimental study was conducted to demonstrate that finned circular and elliptic tubes heat exchangers can be optimized for maximum heat transfer, under a fixed volume constraint. The internal geometric structure of the arrangements was optimized for maximum heat transfer. Better global performance is achieved when flow and heat transfer resistances are minimized together, i.e., when the imperfection is distributed optimally in the available space [1]. Optimal distribution of imperfection represents flow architecture, or constructal design.

The results were presented nondimensionally to permit the general application to heat exchangers of the type treated in this study. A suitable equivalent pressure drop criterion permitted the comparison between circular and elliptic arrangements on a heat transfer basis in the most isolated way possible. The optimal elliptic arrangement exhibits a heat transfer gain of up to 19% relative to the optimal circular tube arrangement. The heat transfer gain and the relative total dimensionless material mass reduction of up to 32% show that the elliptical arrangement has the potential to deliver considerably higher global performance and lower cost.

Three degrees of freedom were investigated in the heat exchanger geometry: tube-to-tube spacing, eccentricity and fin-to-fin spacing. Global optima were found with respect to tube-to-tube spacing, eccentricity and fin-to-fin spacing, i.e., $(S/2b, e, \phi_f)_{opt} \cong (0.5, 0.5, 0.06)$ for $Re_L = 852$ and 1065 . Such globally optimized configurations are expected to be

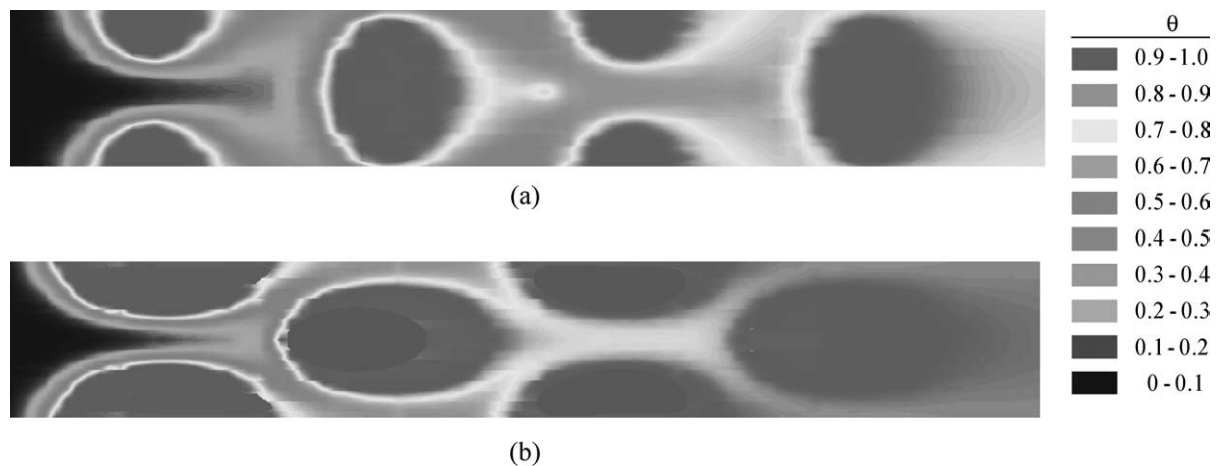


Fig. 12. Fin temperature distribution for four-row tubes and plate fin heat exchangers: (a) $S/2b = 0.5$, $e = 1$, ($\phi_f = 0.006$) and $Re_L = 852$; (b) $S/2b = 0.5$, $e = 0.5$, ($\phi_f = 0.006$) and $Re_L = 852$.

of great importance for actual heat exchangers engineering design, and for the generation of optimal flow structures in general.

Acknowledgements

The authors acknowledge with gratitude the support of the Program of Human Resources for the Oil Sector and Natural Gas, of the Brazilian Oil National Agency—PRH-ANP/MCT. A. Bejan's work was supported by the grant from the National Science Foundation.

References

- [1] A. Bejan, *Shape and Structure*, from Engineering to Nature, Cambridge Univ. Press, Cambridge, UK, 2000.
- [2] H. Brauer, Compact heat exchangers, *Chem. Process Eng.* August (1964) 451–460.
- [3] S.N. Bordalo, F.E.M. Saboya, Pressure drop coefficients for elliptic and circular sections in one, two and three-row arrangements of plate fin and tube heat exchangers, *J. Braz. Soc. Mech. Sci.* XXI (4) (1999) 600–610.
- [4] S.M. Saboya, F.E.M. Saboya, Experiments on elliptic sections in one and two-row arrangements of plate fin and tube heat exchangers, *Exp. Therm. Fluid Sci.* 24 (2001) 67–75.
- [5] J.Y. Jang, J.Y. Yang, Experimental and 3-D numerical analysis of the thermal-hydraulic characteristics of elliptic finned-tube heat exchangers, *Heat Transfer Eng.* 19 (4) (1998) 55–67.
- [6] L.A.O. Rocha, F.E.M. Saboya, J.V.C. Vargas, A comparative study of elliptical and circular sections in one and two-row tubes and plate fin heat exchangers, *Internat. J. Heat Fluid Flow* 18 (1997) 247–252.
- [7] F.E.M. Saboya, E.M. Sparrow, Experiments on a three-row fin and tube heat exchangers, *J. Heat Transfer* 98 (1976) 520–522.
- [8] E.C. Rosman, P. Carajilescov, F.E.M. Saboya, Performance of tube of one and two-row tube and plate fin heat exchangers, *J. Heat Transfer* 106 (1984) 627–632.
- [9] R.S. Matos, J.V.C. Vargas, T.A. Laursen, F.E.M. Saboya, Optimization study and heat transfer comparison of staggered circular and elliptic tubes in forced convection, *Internat. J. Heat Mass Transfer* 20 (2001) 3953–3961.
- [10] O.C. Zienkiewicz, R.L. Taylor, *The Finite Element Method*, vol. 1, McGraw-Hill, London, 1989, Chapter 15.
- [11] G. Stanescu, A.J. Fowler, A. Bejan, The optimal spacing of cylinders in free-stream cross-flow forced convection, *Internat. J. Heat Mass Transfer* 39 (2) (1996) 311–317.
- [12] A.J. Fowler, A. Bejan, Forced convection in banks of inclined cylinders at low Reynolds numbers, *Internat. J. Heat Fluid Flow* 15 (1994) 90–99.
- [13] A. Bejan, *Convection Heat Transfer*, second ed., Wiley, New York, 1995, Chapters 2–3.
- [14] A.J. Fowler, G.A. Ledezma, A. Bejan, Optimal geometric arrangement of staggered plates in forced convection, *Internat. J. Heat Mass Transfer* 40 (8) (1997) 1795–1805.
- [15] J.N. Reddy, D.K. Gartling, *The Finite Element Method in Heat Transfer and Fluid Dynamics*, CRC Press, Boca Raton, FL, 1994, Chapters 4–5.
- [16] T.J.R. Hughes, A simple scheme for developing upwind finite elements, *Internat. J. Numer. Meth. Eng.* 12 (1978) 1359–1365.
- [17] User's manual, AX5810 virtual data logger, AXIOM Technology Co., Ltd, Part 925810, Rev. 1A, Taiwan, 1992.
- [18] User's manual, AX758 16 channel relay multiplexer, AXIOM Technology Co., Ltd, Part 92758, Rev. 2A, Taiwan, 1992.
- [19] L. Howle, J. Georgiadis, R. Behringer, Shadowgraphic visualization of natural convection in rectangular-grid porous layers, *ASME HTD* 206 (1) (1992) 17–24.
- [20] J. Dally, W.F. Riley, K.G. McConnell, *Instrumentation for Engineering Measurements*, Wiley, New York, 1993, p. 425.
- [21] Editorial, Journal of heat transfer policy on reporting uncertainties in experimental measurements and results, *ASME J. Heat Transfer* 115 (1993) 5–6.